JOURNAL OF MATERIALS SCIENCE 39 (2004) 6173–6182

Foreign object damage in disks of gas-turbine-grade silicon nitrides by steel ball projectiles at ambient temperature

S. R. CHOI*,†, J. M. PEREIRA, L. A. JANOSIK, R. T. BHATT
National Aeronautics and Space Administration, Glenn Research Center, Cleveland, Ohio 44135, USA
E-mail: sung.r.choi@grc.nasa.gov

Foreign object damage (FOD) behavior of two commercial gas-turbine-grade silicon nitrides, AS800 and SN282, was determined at ambient temperature through postimpact strength testing of target disks impacted by steel ball projectiles with a diameter of 1.59 mm in a velocity range from 115 to 440 m/s. AS800 silicon nitride exhibited a greater FOD resistance than SN282, primarily due to its greater value of fracture toughness (K_{Ic}). The critical impact velocity V_c for which the corresponding postimpact strength was the lowest was $V_c \approx 440$ and 300 m/s for AS800 and SN282, respectively. A unique lower strength regime was typified for both silicon nitrides depending on impact velocity and was attributed to significant radial cracking. The damage generated by projectile impact was typically in the form of ring, radial, and cone cracks with their severity and combination being dependent on impact velocity. Unlike the thick (3 mm) flexure bar target specimens used in previous studies, the thin (2 mm) disk target specimens exhibited a unique back-side radial cracking on the reverse side just beneath the impact sites at and above impact velocities of 160 m/s for SN282 and 220 m/s for AS800.

1. Introduction

Ceramics, because of their brittle nature, are susceptible to localized surface damage and/or cracking when subjected to impact by foreign objects. It is also true that ceramic components may fail structurally even from the impact of soft particles when their kinetic energy exceeds certain limits. The latter case has been often found in aerospace engines in which combustion products, metallic particles, or small foreign objects cause severe damage to blade/vane components, resulting in serious structural problems. Therefore, foreign object damage (FOD) associated with particle impact needs to be considered when ceramic materials are designed for structural applications. In view of this importance, a considerable amount of experimental and analytical work on impact damage of brittle materials by sharp particles as well as by blunt particles or plates has been accumulated [1–10].

In our previous studies [11, 12], FOD behavior of two representative gas-turbine-grade silicon nitrides, AS800 and SN282, was determined at ambient temperature using flexure bar target specimens. Rigidly supported ceramic target specimens were impacted at their centers by steel ball projectiles with a diameter of 1.59 mm and velocities ranging from 220 to 440 m/s. Postimpact strength of the target specimens was determined as a function of impact velocity to evaluate the severity of impact damage. AS800 silicon nitride exhibited a greater FOD resistance than SN282, due to its greater fracture toughness (K_{Ic}). The fact that K_{Ic} was the key material parameter affecting FOD resistance was further evidenced by the inferior FOD response of an additional equiaxed, fine-grained silicon nitride: this material possessed the lowest fracture toughness of the three silicon nitrides tested in these previous studies. The damage generated by projectile impact was typically in the form of well- or ill-developed ring and cone cracks with a limited occurrence of radial cracks.

The purpose of the present work, as an extension of the previous studies [11, 12], was to investigate FOD behavior of AS800 and SN282 silicon nitrides at ambient temperature using a thin disk configuration of target specimens. The target disks were impacted at their centers at velocities ranging from 115 to 440 m/s by steel ball projectiles with a diameter of 1.59 mm. Postimpact strength of each disk specimen impacted was determined in ring-on-ring biaxial flexure as a function of impact velocity to evaluate the degree of impact damage. Fractography was performed before and after post impact strength testing to determine impact

*Author to whom all correspondence should be addressed.
†NASA Resident Principal Scientist, Ohio Aerospace Institute, Cleveland, OH, USA.

morphologies and the nature of strength-controlling flaw configurations. Full descriptions of this work can be found from a recent report [13].

2. Experimental procedures

2.1. Materials and target specimens

Materials used in this work were the same as those used in our previous work, i.e., commercially available silicon nitrides AS800 (Honeywell, Torrance, CA, '99 vintage, gel-cast) and SN282 (Kyocera, Vancouver, WA, '00 vintage). These two silicon nitrides, both gas-pressure sintered, are currently considered as strong candidate materials for gas-turbine applications in view of their substantially improved elevated-temperature properties [14–16]. Both materials are toughened silicon nitrides with microstructures tailored into elongated grain structures. AS800 silicon nitride has been used at the NASA Glenn Research Center in life prediction programs [17, 18]. The billets for each material were machined into disk target specimens measuring 2.0 mm by 45.0 mm, respectively, in thickness and diameter. The final finishing was completed with a #500 diamond grinding wheel under the specified conditions in accordance with ASTM standard C1161 [19]. Prior to testing, all AS800 target specimens were annealed at 1200°C in air for 2 h to eliminate or minimize damage and/or residual stresses presumably associated with machining. All SN282 specimens were annealed by the manufacturer prior to testing with proprietary annealing condition.

The basic mechanical and physical properties of AS800 and SN282 silicon nitrides as well as of the steel ball projectile material (SAE 52100 chrome steel) are shown in Table I.

2.2. Foreign object damage testing

Foreign object damage (FOD) testing was carried out at ambient temperature using the impact apparatus described in the previous studies [11, 12]. Briefly, hardened (HRC $\geq$ 60) chrome steel balls with a diameter of 1.59 mm were inserted into a 300-mm-long gun barrel with an inner diameter of 1.59 mm. A He-gas cylinder and relief valves were used to pressurize the reservoir to a specific level depending on prescribed impact velocity. Upon reaching a specific level of pressure, a solenoid valve was instantaneously opened accelerating a steel ball projectile through the gun barrel to impact a target specimen that was rigidly supported on an AS800 disk specimen (in 2-mm thickness and 45-mm diameter) backed on a rigid metallic specimen holder. Each target specimen was aligned such that the projectile impacted the center of the test specimen at an incidence angle normal to the surface. For a given pressure, the velocity of each steel projectile was determined using two pairs of transmitter and receiver lasers, in which the two transmitters were aimed at the respective receivers through two holes in the gun barrel. The impact velocity applied in this work ranged from 115 to 440 m/s. Typically, 10 test specimens were impacted at each chosen velocity for a given material. Impact morphologies at both impact site and back side of each impacted specimen were examined optically right after impact testing but prior to strength testing.

2.3. Postimpact strength testing

Strength testing for impacted disks was performed in ambient-temperature air using a steel ring-on-ring biaxial flexure fixture with 20-mm load-ring and 40-mm support-ring diameters. A series of steel balls were used to eliminate frictional constraint at each of the load and support rings, similar to a thrust ball bearing assembly. Note that a continuous ring configuration, analogous to four-point flexure with fixed rollers, has exhibited fictional constraint as a source of stress error. Each impact-tested specimen was coaxially located in the biaxial flexure fixture such that its impact site was placed in tension. An electromechanical test frame (Model 8562, Instron, Canton, MA) was used in displacement control with an actuator speed of 0.5 mm/min. A fractographic analysis was performed after strength testing to determine failure origin, flaw configuration, mode of fracture and crack branching behavior. The as-received biaxial fracture strength was also determined for each material

TABLE I Basic mechanical and physical properties of AS800 and SN282 silicon nitrides and steel-ball projectiles at ambient temperature [12]

					Flexure strength[d]			
Material	Elastic modulus[a] E (GPa)	Poisson's ratio[a] ν	Density[b] ρ (g/cm^3)	Hardness[c] H (GPa)	Mean strength (MPa)	Weibull modulus	Characteristic strength (MPa)	Fracture toughness[e] K_{IC} (MPa$\sqrt{}$m)
AS800 Si_3N_4	309	0.27	3.27	13.6(1.4)	775 (45)[g]	21	795	8.1 (0.3)
SN282 Si_3N_4	304	0.28	3.32	15.3 (0.2)	595 (64)	11	623	5.5 (0.2)
Chrome steel balls (SAE 52100)	200[f]	0.30[f]	7.80	HRC $\geq$ 60[f]	–	–	–	–

[a]By the impulse excitation technique, ASTM C 1259 [19].
[b]By mass/volume method.
[c]By Vickers microhardness indentation, ASTM C 1327 [20].
[d]By four-point flexure with 20/40 mm spans, ASTM C1161 [18]. A total of 20 test specimens used for each material.
[e]By single-edge-precracked-beam (SEPB) method, ASTM C 1421 [21].
[f]From the manufacturer's data; HRC = Hardness in Rockwell C scale.
[g]The numbers in the parentheses indicate $\pm$1.0 standard deviations.

with 8 to 10 test specimens using the same test fixture, test frame, and test conditions that were utilized for the postimpact strength testing.

3. Results and discussion

3.1. Strength

3.1.1. As-received biaxial strength

The two-parameter Weibull plots of as-received biaxial fracture strengths of both AS800 and SN282 silicon nitrides are shown in Fig. 1, where $\ln\ln[1/(1-F)]$ was plotted as a function of $\ln\sigma_f$ with F and σ_f being failure probability and biaxial fracture strength, respectively. The number of specimens used in the biaxial fracture strength data was 10 and 21, respectively, for AS800 and SN282. Weibull modulus m and characteristic strength σ_θ were $m = 18$ and $\sigma_\theta = 698$ MPa for AS800. For SN282, $m = 8$ and $\sigma_\theta = 451$ MPa. The mean strength was 678 $\pm$ 45 MPa for AS800 and 426 $\pm$ 60 MPa for SN282. The Weibull modulus for AS800 and SN282 ($m = 18$ and 8, respectively) in biaxial configuration compares well with the values determined previously ($m = 21$ and 11, respectively, see Table I) for AS800 and SN282 in uniaxial four-point configuration [12]. Failure origins of both silicon nitrides, in many cases, were associated with surface-related defects such as machining flaws, pores, and elongated grains.

3.1.2. Postimpact strength

The results of strength testing for impacted target specimens are shown in Fig. 2, where postimpact biaxial fracture strength was plotted as a function of impact velocity for both silicon nitrides. The biaxial fracture strength of both as-received materials was also included for comparison. Frequently, the specimens impacted at low velocities did not incur fractures originating from the impact sites and were indicated with closed symbols in the figure. For AS800, two specimens out of ten did not obtain fractures originating from the impact sites when impacted at 220 m/s. For SN282, one, two, four, and nine (each out of ten) specimens did not fail from

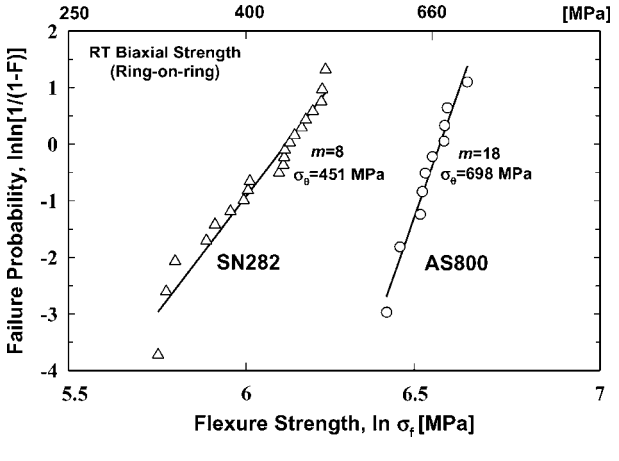

Figure 1 Weibull distributions of biaxial strength of as-received AS800 and SN282 silicon nitrides disks determined in ring-on-ring biaxial flexure at ambient temperature. The lines represent the best-fit.

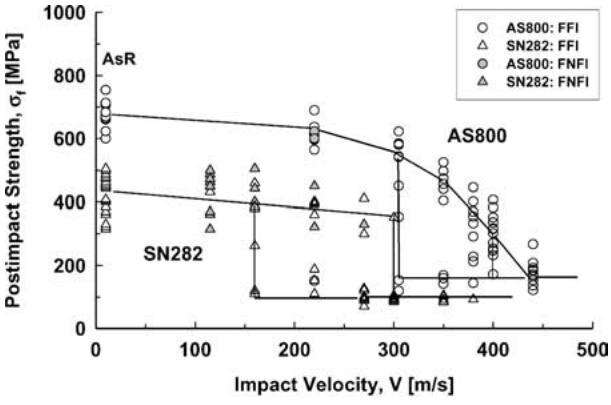

Figure 2 Postimpact biaxial strength as a function of impact velocity, determined for AS800 and SN282 silicon nitrides disks impacted by steel ball projectiles with 1.59-mm-diameter steel ball projectiles at ambient temperature. "AsR" indicates as-received biaxial flexure strength of each material. The bottom lines indicate the lower strength regime. Open symbols: failed from impact sites ("FFI"); Closed symbols: failed not from impact sites ("FNFI").

the impact at 270, 220, 160, and 115 m/s, respectively. Those specimens not failing from fractures initiating at the impact sites were equivalent in strength to the corresponding as-received specimens and thus were used to provide valid data in estimating the overall as-received biaxial fracture strength for each material.

As seen in the figure, the postimpact strength, in general, decreased with increasing impact velocity. Unlike the postimpact strength of flexure bars [11, 12], the postimpact biaxial strength for a given impact velocity (greater than 220 and 160 m/s for AS800 and SN282, respectively) was typified with two distinct regions of strength: higher and lower strength regimes. The strength of the lower regime was around 150 and 100 MPa for AS800 and SN282, respectively. The lower strength regime started at 300 m/s and 160 m/s for AS800 and SN282, respectively. The postimpact strength of each material converged to this lower regime strength as impact velocity sufficiently increased. This velocity at which a minimum (or the lowest) postimpact strength was retained is called the "critical impact velocity" (V_c) and was found to be the following:

$$V_c \approx 440 \text{ m/s} \quad \text{for AS800}$$
$$V_c \approx 300 \text{ m/s} \quad \text{for SN282}$$

These critical impact velocities for disks are in good agreement with those for flexure bars, for which $V_c \approx$ 400 and 300 m/s were observed for AS800 and SN282, respectively [11, 12]. In the case of flexure bars, the target specimens failed upon impact at the critical impact velocity yielding a zero strength due to their small width (4 mm), whereas the disk specimens did not fracture upon impact but instead exhibited a significant size of radial cracks while retaining the lower regime strength in strength testing because of their relatively large disk diameter (45 mm) compared to the size of the radial cracks. The results in Fig. 2 lead to a conclusion that resistance to FOD is greater in AS800 than in SN282, due to greater fracture toughness in AS800, consistent

with the previous FOD results on flexure bar specimens [11, 12].

3.2. Impact morphology and fractography

3.2.1. Steel ball projectiles

The hardened steel ball projectiles were flattened after impact mainly at lower impact velocities. The flattened surfaces of the steel ball projectiles retained the impression of the machining marks of ceramic target specimens with a series of numerous parallel lines, indicative of the significant severity of plastic deformation. At higher impact velocities, the projectiles were subjected to extreme heat and severe cracking, and even sparks were frequently observed from the impact sites on the onset of impact.

3.2.2. Target specimens

3.2.2.1. Impression marks. The impression marks, generated because of material transfer upon impact from steel ball projectiles to ceramic target specimens in a phenomenon known as a cold welding, exhibited a unique feature such that they were in the form of rings, having inner and outer diameters, as seen in Fig. 3. The impression marks were either not visible or not produced on the specimens impacted below 220 m/s, attributed to insufficient impact force to cause cold welding. At higher impact velocities of 400 to 440 m/s for AS800, significant material transfer was observed with a sign of outward splashing of metal. The measurements of the impression marks for both silicon nitrides are shown in Fig. 3b. The measurements were made using a total of 5 to 10 specimens at each impact velocity. The outer diameter d_o increased with increasing impact velocity for both silicon nitrides, approaching approximately the diameter of projectile; whereas the inner diameter remained almost constant with an average of $d_i = 0.82 \pm 0.07$ mm, regardless of impact velocity. It is natural to consider that the outer diameter of impression would correspond to the outside diameter of ball projectile upon impact and that it would increase with increasing impact velocity. However, the unchanging nature of inner diameter with increasing impact velocity as well as the occurrence of ring shape on impact sites imposes a difficulty in understanding the details of the deformation mechanism(s) involved therein.

The tensile principal stress, according to the Hertzian contact analysis, occurs just outside the area of contact between two contacting elastic bodies in which a cone crack initiates and propagates through the locus of maximum tensile stress [5, 9]. In cases of impacts with hard projectiles and hard target materials (such as ceramic balls and ceramic target materials), it has been shown that agreement between the calculated contact area (radius) and the upper size (radius) of a cone was reasonable [4]. The contact area can be estimated based on the Hertzian contact theory together with the principle

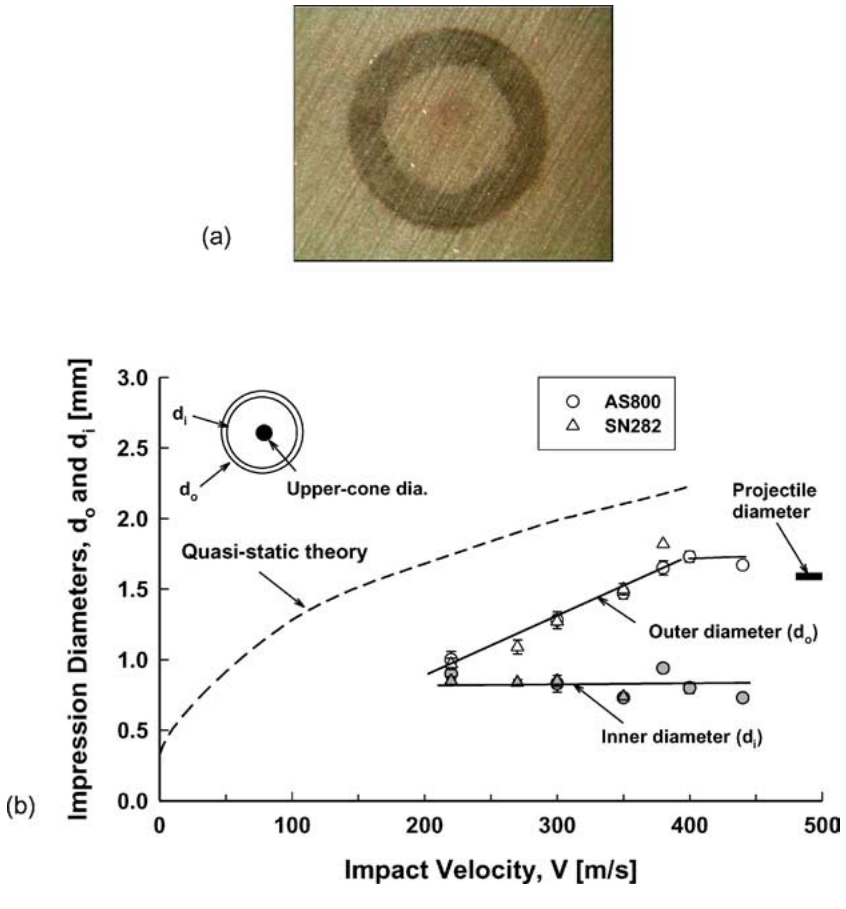

Figure 3 (a) A typical impression mark sowing a ring shape from the impact site of a AS800 silicon nitride disk impacted by 1.59-mm-diameter steel ball projectiles impacted at 350 m/s; (b) Impression size as a function of impact velocity for AS800 and SN282. The contact-area size ($2a$) estimated by the quasi-static contact theory, Equation 1, is included for comparison. Open symbols for d_o; closed symbols for d_i.

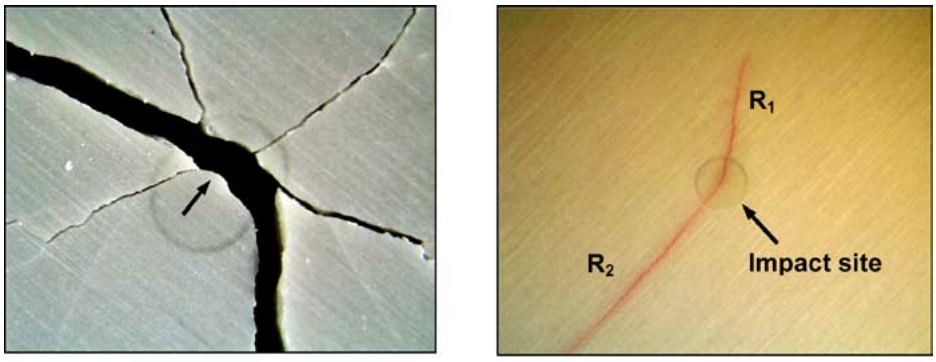

Figure 4 (a) A typical example of an AS800 silicon nitride disk failed from a ring crack in postimpact strength testing. Impact velocity = 220 m/s; postimpact strength = 616 MPa; (b) A typical example showing significant radial cracks in an AS800 disk, situated in the lower strength regime. Impact velocity = 220 m/s; post-impact strength (controlled by the 4.7-mm crack R_2) = 151 MPa .

of conservation of impact energy as follows [1, 4, 5, 8]:

$$a = \alpha(k/E)^{1/5}\rho^{1/5}RV^{2/5} \tag{1}$$

where a is the radius of contact area, α is a constant ($\approx$1.3), E is the elastic modulus of the target material, ρ is the density of the projectile, R is the radius of projectile, and V is the impact velocity. The parameter k is expressed as

$$k = (1 - \nu^2) + (1 - \nu'^2)\frac{E}{E'} \tag{2}$$

with ν being Poisson's ratio and the primes denoting variables associated with the projectile. As shown in Fig. 3b, the calculated contact area $2a$ based on Equation 1 was significantly greater than the impression sizes observed. However, it should be noted that a direct comparison should not be made between the calculated and the observed values since the calculated impression size was unrealistically large, indicating that the calculated values were in the range of significant plastic deformation. As a consequence, the impact events in this work can be characterized as plastic (in projectile)-elastic (in target material) rather than elastic-elastic impact that is the case for ceramic balls vs. ceramic target.

3.2.2.2. Impact sites and fracture surfaces. At lower impact velocities, both AS800 and SN282 specimens failed similarly from ring cracks, in which a part of the ring contour was seen at failure origin as a small curved portion, as shown in Fig. 4. At intermediate impact velocities, ring or radial cracks were associated with failure. The upper cones located at the impact center, whether somewhat well developed or not, seemed to be rarely associated with failure origins. Failure location as a function of postimpact strength, determined for the specimens failing from ring cracks, showed that an average value of failure location from the impact center was 0.28 $\pm$ 0.07 mm (or 0.56-mm diameter). This indicates that the strength-controlling ring cracks were situated between the inner diameter (0.82 mm) of impression and the outside of the upper cone diameter (0.23 mm, determined individually). The lower strength regime, typified at intermediate velocities of each material, was associated exclusively with well-developed radial cracks ranging in size from 3 to 5 mm, emanating from the impact sites, as shown in Fig. 4b. These radial cracks resulted in the lower strength regime around 150 and 100 MPa, respectively, for AS800 and SN282. Hence, it is important to note that the existence of lower strength regime was due to the occurrence of these significant radial cracks.

At higher impact velocities close to or above the critical impact velocity, failure of both materials was mainly associated with well-developed radial cracks even though well-developed cone cracking invariably occurred simultaneously. In many cases, cones with lower diameters ranging from 4 to 6 mm were separated from the specimen after strength testing. A typical impact site showing the impression, radial cracks, and an upper cone together with a back-side view, a fracture surface, and a separated cone is shown in Fig. 5. The dimensions of the cones, including upper and lower diameters and heights, were determined for both silicon nitrides from either fracture surfaces or separated cones using typically seven specimens in measurements at each impact velocity. The cone angle, defined as half of apex angle, was calculated based on the determined cone geometry.[1] The cone angle with an average value of 42 $\pm$ 2° remained almost unchanged regardless of material over impact velocities from 350 to 440 m/s. There is limited information in the literature on cone angles resulting from impact of a ceramic target by steel ball projectiles, and it is available only as photographs [e.g., 23], so a meaningful comparison between this work and the published data could not be made. However, it should be noted that the angle also depends on variables such as specimen geometry, type of specimen support, projectile material, and impact velocity.

Fig. 6 shows the probability of occurrence of radial cracks as a function of impact velocity, determined with a total of 10 disks at each velocity for a given material. For a given impact velocity, the occurrence of radial cracking was greater in SN282 than in AS800, attributed to lower fracture toughness in SN252 (see

[1] Strictly speaking, the cones were not straight but a little curved particularly toward their bottom. The calculation of cone angle, however, was made based on the straight line extended to the bottom in some cases.

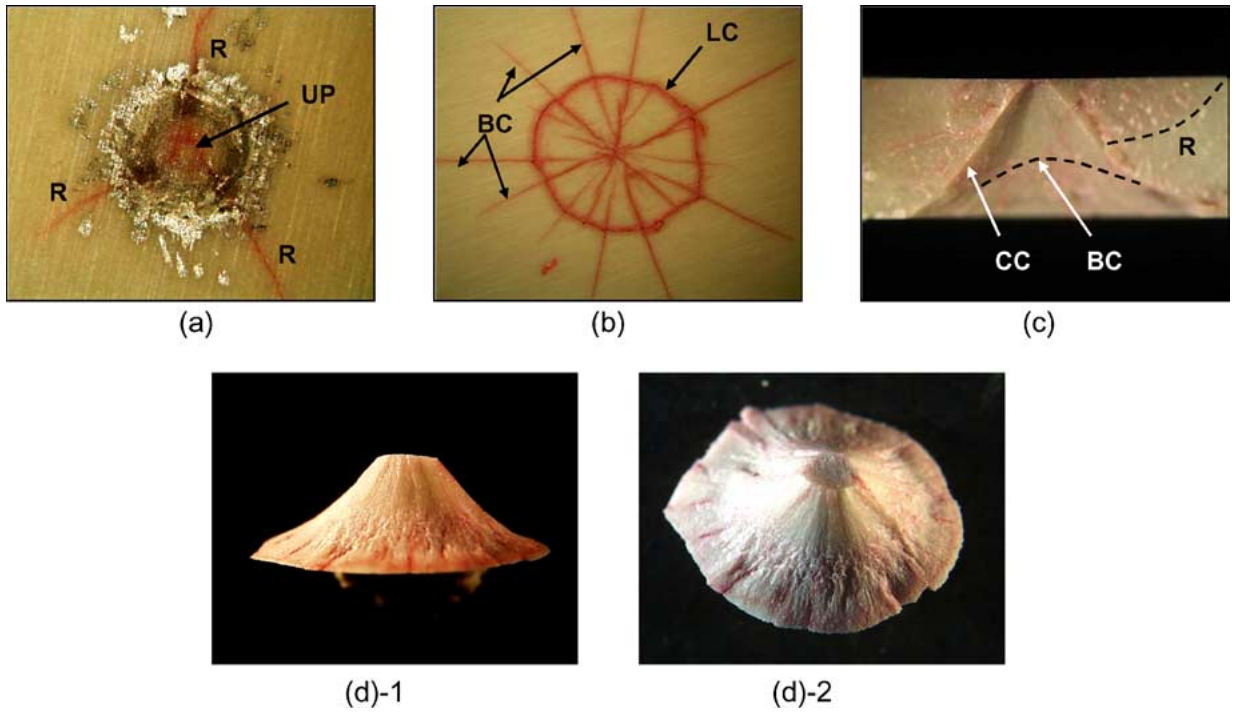

Figure 5 Typical examples of impact damages occurring in an AS800 silicon nitride disk impacted at 440 m/s: (a) impact site showing impression, radial cracks (R), and upper cone (UP) before strength testing; (b) backside view showing backside radial cracks (BC, radiating from the center) and lower diameter of a cone (LC) before strength testing; (c) fracture surface showing a cavity of a cone (CC), impact-site (upper) radial cracks (R), and backside radial cracks (BC); (d) side and top views of a cone separated from (c). Post-impact strength = 192 MPa.

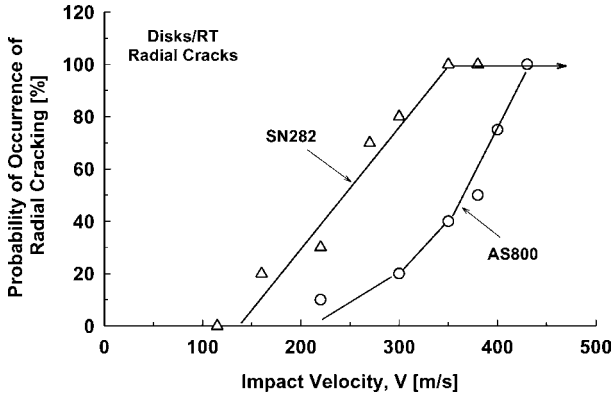

Figure 6 Probability of occurrence of radial cracking as a function of impact velocity for AS800 and SN282 silicon nitrides disks impacted by 1.59-mm-diameter steel ball projectiles.

Table I). The figure also indicates that the critical impact velocity, 300 and 440 m/s for SN282 and AS800, respectively, corresponds to the case where the probability of occurrence is close to 100 percent for each material.

3.2.2.3. Back-side cracking. Unlike flexure bar specimens, disk target specimens exhibited a peculiar feature of back-side cracking that occurred on the reverse side of disks depending on impact velocity. Typical back-side cracking generated upon impact—but prior to postimpact strength testing—and the corresponding fracture surface are shown in Fig. 7. Well-defined and somewhat symmetric radial cracks originated in the reverse side of the specimen from a point just beneath the impact site. The crack configuration was semi-elliptical with a minor to major axis ratio of around 0.2 to 0.3. The occurrence of back-side cracking increased with higher impact velocity, as shown in Fig. 8. For a given impact velocity, the probability of occurrence of back-side cracking was a little greater in SN282 than in AS800, again due to lower fracture toughness in SN282 than in AS800. The sizes of maximum back-side cracks, measured from its center, are shown in Fig. 8b. AS800 showed almost consistent crack size independent of impact velocity with a mean size of around 6 mm, whereas SN282 showed a somewhat dependency of crack size on impact velocity. The reason for the occurrence of back-side cracking in disk target specimens will be discussed later in Section 3.3.

3.2.2.4. Fracture map. As mentioned above, several different types of damage and/or cracking including ring, radial, cone, and back-side cracks were generated in disk target specimens individually or simultaneously, depending on impact velocity. Fig. 9 show a fracture map, which summarizes the types of damage and/or cracks with respect to impact velocity for both AS800 and SN282 silicon nitrides. For each material at its respective low impact velocities, the occurrence of ring cracks was dominant. At intermediate velocities, ring with either radial or cone (a rare case) cracks are prevalent. Either ring or radial cracks determine the postimpact strength depending on the impact velocity, with radial cracking becoming the dominant influence as impact velocity increases. At or above the critical impact velocities, both well-developed radial and cone cracks occur; however, radial cracks uniquely control the postimpact strength.

Fig. 9 also includes the range of impact velocities where back-side radial cracking for each silicon nitride

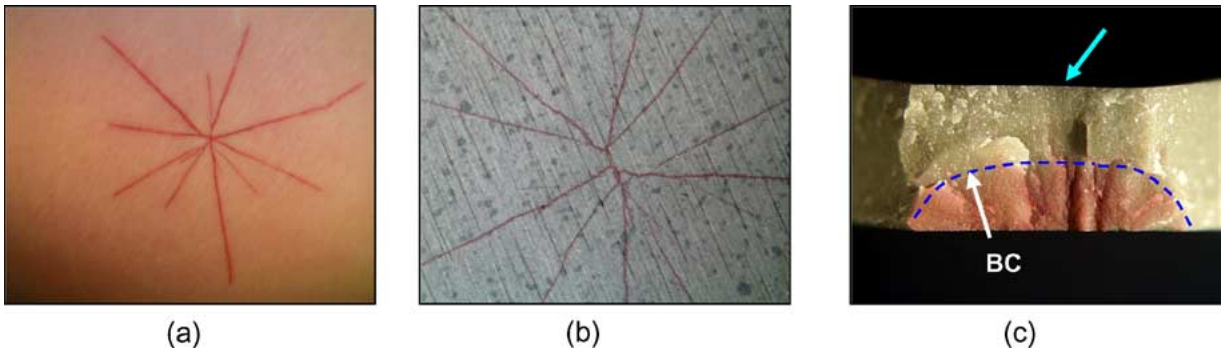

Figure 7 Typical examples of well-developed back-side radial cracking and fracture surface: (a) AS800 silicon nitride disk impacted at 300 m/s (before strength testing); (b) SN282 silicon nitride disk impacted at 300 m/s (before strength testing); (c) fracture surface of the AS800 specimen (in (a)) showing back-side cracks (BC) and a failure origin with an arrow. The corresponding post-impact strength was 450 and 96 MPa, respectively, for AS800 (in (a)) and SN282 (in (b)) specimens.

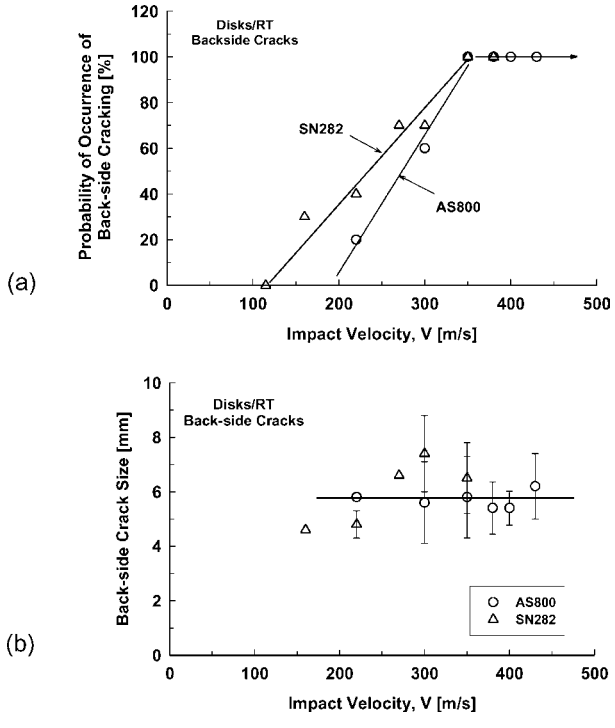

Figure 8 (a) Probability of occurrence of back-side cracking and (b) size of back-side cracks, as a function of impact velocity for AS800 and SN282 silicon nitrides disks impacted by 1.59-mm-diameter steel ball projectiles.

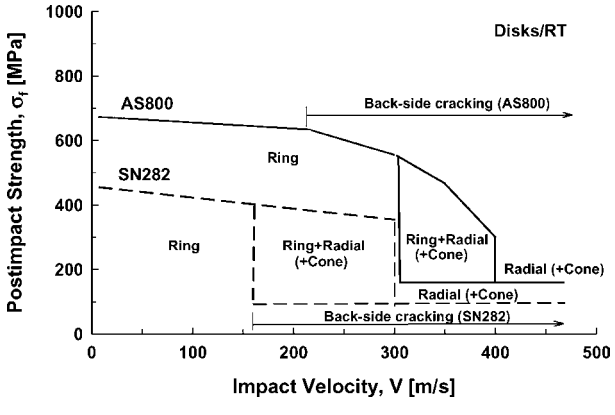

Figure 9 Fracture map constructed for AS800 and SN282 silicon nitrides disks impact by 1.59-mm-diameter steel ball projectiles at ambient temperature. The range of impact velocity for back-side cracking is also included. "(+Cone)" represents cone cracking but not associated with strength controlling flaws.

takes place. Although cone cracks wouldn't affect component strength significantly in view of their geometry and size compared with the severity of radial cracks, they are responsible for material loss when the cones are formed through the thickness of a component and then separated from the component. This problem would be significant if one of the requirements of the component is some type of sealing, separation, and/or environmental barriers.

3.3. Analytical considerations

3.3.1. Strength degradation

A phenomenological model of strength degradation due to ball impact was proposed previously by Wiederhorn and Lawn [1], based on assumptions that the impact event was elastic and quasi-static and that strength degradation was attributed to the formation of cone cracks. Also, another important assumption was that the size for strength-controlling flaws to be effective was proportional to the base radius of the cone [1, 5, 9]. With those assumptions, strength degradation was modeled using Hertzian contact analysis, the principle of energy conservation, and indentation fracture relations. The model, despite several assumptions, was in good agreement with experimental dada determined for glass impacted by steel or tungsten carbide spherical projectiles [1]. The resulting strength degradation as a function of impact velocity is expressed as follows [1]:

$$\sigma_f = \Phi(k/E)^{2/15}\rho^{-1/5}R^{-2/3}K_{IC}^{4/3}V^{-2/5} \qquad (3)$$

where Φ is a parameter associated with the projectile geometry and K_{IC} is fracture toughness. Equation 3 can also be expressed in terms of impact kinetic energy (U_K) to yield

$$\sigma_f = \Phi'(k/E)^{2/15}R^{-1/15}K_{IC}^{4/3}U_K^{-1/5} \qquad (4)$$

where $\Phi' = (2\pi/3)^{1/5}\Phi$ and $U_K = mV^2/2$ with m being mass of a projectile.

The average postimpact strength (log σ_f), reconstructed from Fig. 1 with higher and lower strength regimes, were plotted as a function of impact kinetic energy (log U_K) in Fig. 10. It is noted from the figure

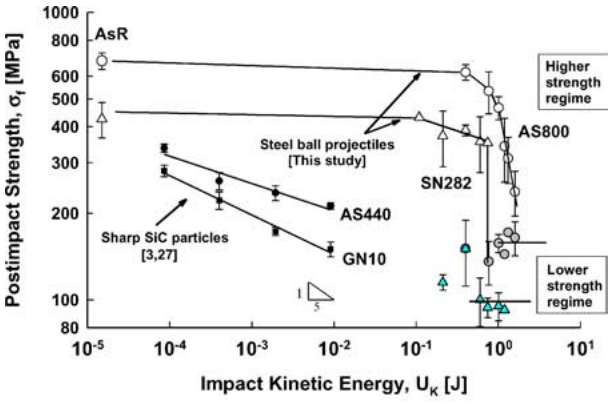

Figure 10 Postimpact biaxial strength as a function of impact kinetic energy for AS800 and SN282 silicon nitrides impacted by steel ball projectiles. The postimpact biaxial strength data on "sharp" SiC particle impact for AS440 and GN10 silicon nitrides [3, 27] were included for comparison. The higher and lower strength regimes are indicated. The error bars indicate ±1.0 standard deviations. The theoretical slope of −1/5 is also indicated.

that the discrepancy in slope between the prediction of $-1/5$ and the experimental data seemed insignificant at impact energy of $U_K < 0.8$ J ($V < 300$ m/s) for both AS800 and SN282, except for the lower strength regime of SN282. However, the discrepancy was significant above $U_K > 0.8$ J for AS800 at the higher strength regime while it was already significant at the lower strength regime for SN282, i.e., $V \geq V_c$. The strength degradation model (Equation 3 or 4) assumed that cone cracks are dominant strength-controlling flaws. However, as seen in this work (e.g., see the fracture map in Fig. 9), cone cracking was not uniquely involved in impact event; rather, several different types of flaws were associated individually or simultaneously, depending on impact velocity. Hence, the cone-cracking model, Equation 3 or 4, would not be appropriate to describe the postimpact biaxial strength behavior of AS800 and SN282 silicon nitrides, as also observed previously from uniaxial flexure beam target specimens [11, 12]. Part of the reason comes from the significant plastic deformation of a projectile upon impact, deviating remarkably from the model's assumption of idealized elastic impact.

3.3.2. Back-side cracking

As mentioned in Experimental Procedures, the disk specimens in this work were placed on an extra AS800 disk backed by a bulky steel bracket. Hence, the specimens were considered to be rigidly supported over their whole area. However, as seen from Fig. 7, well-developed back-side cracking took place, as if the specimens had been supported only over their circumferences [e.g., 24]. A most plausible reason for the back-side cracking would be derived from a concept of *elastic foundation*. This comes from the idea that although the specimens were rigidly supported, they—because of significant impact force—might act like ones supported on elastic foundation, and any deflection of elastic foundation due to impact results in bending of the specimens, which will cause a localized tensile stress field on the reverse side of the specimens. The solutions of the elastic foundation effect are very complex and require a detailed elastic spring constant of the foundation that is a combined AS800 and steel bracket in this case.

With some simplifying assumptions, the maximum tensile stress on the back side of the disks occurring upon impact was estimated based on the elastic foundations approach [25]. The following assumptions were made in the analysis:

(1) The pressure developed at any point between the beam and the foundation is proportional to the deflection of the beam at that point (see Fig. 11).
(2) The specimen is considered as infinite beam subjected to a concentrated load for a conservative approach.
(3) The impact force acts as a concentrated load.
(4) The impact force can be estimated based on the quasi-static contact theory by [1, 4, 5, 8]:

$$P = \alpha(k/E)^{-2/5}\rho^{3/5}R^2V^{6/5} \tag{5}$$

The maximum tensile stress σ_{max} occurring in the tension side of the beam opposite to the load point is given with other parameters as follows [25]:

$$\sigma_{max} = \frac{M_{max}c}{I}$$

$$M_{max} = \frac{P}{4\beta}C_{\beta z}$$

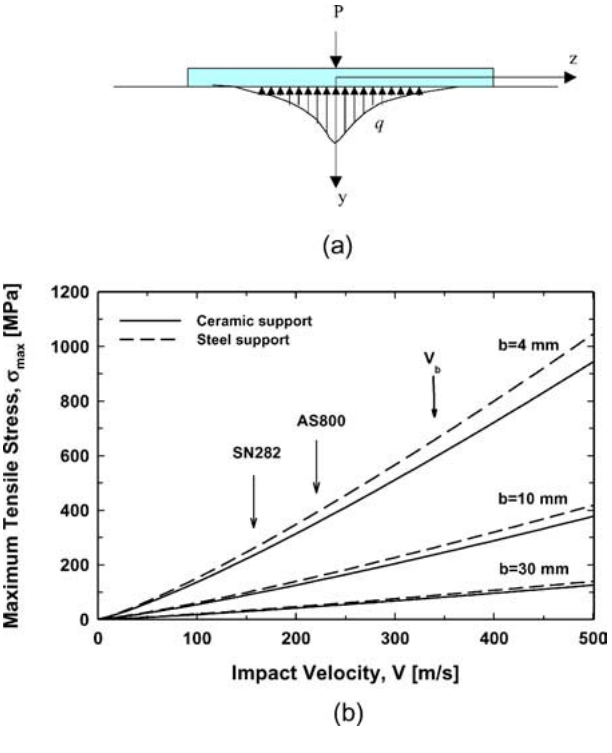

Figure 11 (a) Geometry of elastic foundation; (b) Maximum tensile stress as a function of impact velocity, occurring on the reverse side of a disk at a point opposite to impact site, based on the elastic foundation approach [25]. The initiation velocity for back-side cracking is indicated as an arrow for each material. V_b is a velocity (=350 m/s) that resulted in 100% backside cracking for both silicon nitrides.

$$y = \frac{P\beta}{2k} A_{\beta z} \tag{6}$$
$$\beta = \sqrt[4]{\frac{k}{4EI}}$$
$$k = bk_o$$

where

$$A_{\beta z} = e^{-\beta z}(\sin \beta z + \cos \beta z)$$
$$C_{\beta z} = e^{-\beta z}(\cos \beta z - \sin \beta z) \tag{7}$$

where M_{max} is the maximum bending moment, c is the half of specimen depth, I is the second moment of inertia of a beam, y is the beam deflection, k_b is the spring constant over the width of the foundation, k_0 is the spring constant of foundation, and b is the beam width. The maximum bending moment (and thus stress and deflection) occurs at the load point, i.e., $z = 0$; hence, $A_{\beta z} = C_{\beta z} = 1.0$. Two different elastic supports of silicon nitride ($E = 300$ GPa) and steel ($E = 200$ GPa) disks, placed on an infinitely rigid body, were considered in this estimation. The spring constants of the elastic supports were taken as $k_0 = 2 \times 10^8$ and 1.3×10^8 N/mm for silicon nitride and steel supports, respectively, based on their Young's modulus values and geometry (2-mm thickness and 40-mm diameter). Three different beam widths of $b = 4$, 10, and 30 mm were considered.

The results of maximum tensile stress estimated using Equation 6 are shown in Fig. 11. For $b = 10$ mm, smaller than target specimen's diameter, the maximum tensile stresses at $P = 25$ kN that correspond to the case ($V_b = 350$ m/s) where all AS800 and SN282 disks exhibited back-side cracking (see Fig. 8), were 240 and 270 MPa, respectively, for silicon nitride and steel supports. For $b = 30$ mm, which might better represent the actual target specimen diameter, the respective maximum tensile stresses were 80 and 90 MPa. Hence, the estimated maximum tensile stress based on the elastic foundation approach was much lower than the target material's strength and consequently, insufficient to cause back-side cracking. Although several simplifying assumptions were used in the estimation, and their justification must be verified, the elastic foundation approach gives an insight into the reason for the occurrence of back-side cracking at least quantitatively. The back-side cracking was also observed recently for rigidly supported intermetallic disks such as MoSiB and NbSi, subjected to impact by steel ball projectiles of 1.59 mm diameter [26].

3.4. Comparison in FOD behavior

3.4.1. Steel-ball projectile vs. hard-sharp particle

A comparison of postimpact biaxial strength of silicon nitrides between blunt steel ball impact (this study) and sharp SiC-particle (16 and 46 grit) impact [3, 27] is also shown in Fig. 10. Note a considerable strength degradation for the case of sharp particle impact occurring even at much lower impact kinetic energy, showing that the severity of impact damage was far greater in "sharp" particle impact than in "blunt" (steel ball) projectile impact. The sharp particle impact typically produced radial cracks emanating from the impact sites (similar to the Vickers indent cracks that originate from the corners of an impression site), thereby resulting in significant strength degradation. The results in the figure show again that for a given target material and a given impact energy, the geometry and material of projectiles are very important parameters affecting the postimpact strength behavior of advanced ceramics.

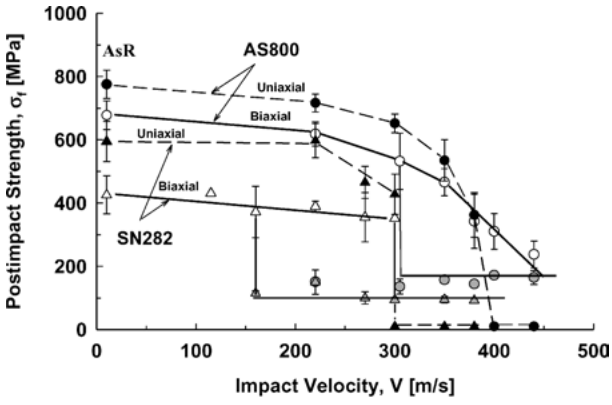

Figure 12 Comparison of post-impact strength as a function of impact velocity between flexure bars [11,12] and biaxial disks [this study] of AS800 and SN282 silicon nitrides impacted by 1.59-mm-diameter steel ball projectiles at ambient temperature. "AsR" indicates as-received flexure strength of both materials. The error bars indicate ±1.0 standard deviations.

3.4.2. Disks vs. flexure bars

Fig. 12 also shows a comparison of postimpact strength behaviors between the biaxial disks (2-mm thickness and 45-mm diameter) in this work and the uniaxial flexure bars (4 by 3 by 45 mm in width, depth, and length, respectively) in the previous work [11, 12]. Both disks and flexure bars were rigidly supported, and the same steel ball projectiles were used. The overall postimpact strength was higher for uniaxial flexure bars than for biaxial disks because of the size effect.[2] The critical impact velocity for uniaxial bars was $V_c \approx 300$ and 400 m/s for SN282 and AS800, respectively, while for biaxial disks it was $V_c \approx 300$ and 440 m/s, resulting basically in good agreement in V_c between the two different specimen configurations. However, the lower strength regime uniquely occurring in biaxial disks was not seen in uniaxial flexure bars, primarily due to the difference in specimen thickness: thin (disks) versus thick (flexure bars). Furthermore, the back-side cracking characterizing biaxial disks was not exhibited in

[2] A prediction of strength from one specimen configuration (uniaxial) to another (biaxial) was made using the principle of independent action (PIA, Weibull statistics) with surface flaws for as-received specimens. The ratio of predicted biaxial to uniaxial strengths (as-received) was 0.90 and 0.82 for AS800 and SN282, respectively, whereas the ratio of actual biaxial and uniaxial strengths was found to be 0.89 and 0.72. From excellent to reasonable agreement was found for AS800 and SN282 specimens, respectively. The Weibull moduli in this prediction were taken as $m = 20$ and 10 for AS800 and SN282, respectively.

the flexure bars, possibly again due to the difference in specimen thickness, as noted by the elastic foundation approach (with strength depending on [1/(thickness)^2]). Although the general trend of postimpact strength with respect to impact velocity seemed similar in both specimen configurations, the occurrence of significant radial and back-side cracking was very different from one specimen configuration to another even using the same target material under the same impact conditions. This implies that a particular set of impact data generated under particular impact conditions may not be universally applicable to a variety of applications. A case-by-case approach must be sought.

4. Conclusions

Based on the results of FOD testing using biaxial target disks at ambient temperature for two in-situ toughened, gas-turbine-grade silicon nitrides (AS800 and SN282), following conclusions were made:

1. The overall FOD resistance was greater for AS800 silicon nitride than for SN282 silicon nitride, primarily due to greater value of fracture toughness in AS800.
2. The critical impact velocities, in which biaxial target disks exhibited the lowest postimpact strength, were about 440 and 300 m/s, respectively, for AS800 and SN282. The occurrence of critical impact velocity was associated with the generation of significant sizes (5 to 7 mm) of radial cracks originating from the impact sites.
3. As impact velocity increased, more different crack types were involved in the impact event, occurring either individually or simultaneously. A fracture map was proposed to identify the occurrence of particular crack systems including ring, radial, cone, and back-side cracking with respect to impact velocity.
4. In terms of the different specimen geometries and configurations, the degree of additional damage by radial and back-side cracking was much more severe in thin biaxial specimens than in thick uniaxial flexure bars. This indicates that a particular set of impact data generated under particular impact conditions may not be universally applicable to a variety of applications. A case-by-case approach to specific geometries and configurations should be taken into consideration.

Acknowledgements

The authors are thankful to R. Pawlik for the experimental work during the course of this study. This work was supported by the Higher Operating Temperature Propulsion Components (HOTPC) Program, currently the Ultra-Efficient Engine Technology (UEET) Program, NASA Glenn Research Center.

References

1. S. M. WIEDERHORN and B. R. LAWN, *J. Amer. Ceram. Soc.* **60**(9/10) (1977) 451.
2. *Idem.*, *ibid.* **62** (1/2) (1979) 66.
3. J. E. RITTER, S. R. CHOI, K. JAKUS, P. J. WHALEN and R. G. RATEICK, *J. Mater. Sci.* **26** (1991) 5543.
4. Y. AKIMUNE, Y. KATANO and K. MATOBA, *J. Amer. Ceram. Soc.* **72**(8) (1989) 1422.
5. C. G. KNIGHT, M. V. SWAIN and M. M. CHAUDHRI, *J. Mater. Sci.* **12** (1977) 1573.
6. M. RAJENDRAN and J. L. KROUPA, *J. Appl. Phys.* **66**(8) (1989) 3560.
7. L. N. TAYLOR, E. P. CHEN and J. S. KUSZMAUL, *Comp. Meth. Appl. Mech. Eng.* **55** (1986) 301.
8. R. MOUGINOT and D. MAUGIS, *J. Mater. Sci.* **20** (1985) 4354.
9. G. EVANS and T. R. WILSHAW, *ibid.* **12** (1977) 97.
10. M. LIAW, A. S. KOBAYASHI and A. G. EMERY, *J. Amer. Ceram. Soc.* **67** (1984) 544.
11. S. R. CHOI, J. M. PEREIRA, L. A. JANOSIK and R. T. BHATT, *Ceram. Eng. Sci. Proc.* **23**(3) (2002) 193.
12. S. R. CHOI, J. M. PEREIRA, L. A. JANOSIK and R. T. BHATT, "NASA/TM-2002-211821, National Aeronautics & Space Administration" (Glenn Research Center, Cleveland, OH, 2002).
13. S. R. CHOI, J. M. PEREIRA, L. A. JANOSIK and R. T. BHATT, "NASA/TM-2003-212224, National Aeronautics & Space Administration" (Glenn Research Center, Cleveland, OH, 2002).
14. T. OHJI, *Ceram. Eng. Sci. Proc.* **22**(3) (2001) 159.
15. F. LOFAJ, S. M. WIEDERHORN and P. R. JEMIAN, *ibid.* **22** (3) (2001) 167.
16. H. T. LIN, S. B. WATERS, K. L. MORE, J. WIMMER and C. W. LI, *ibid.* **22**(3) (2001) 175.
17. S. R. CHOI and J. P. GYEKENYESI, (a) *ASME J. Eng. Gas Turbines & Powers* **121** (1999) 18; (b) in "Fracture Mechanics of Ceramics," Vol 13, edited by R. C. Bradt, D. Munz, M. Sakai, V. Ya. Shevchenko and K. W. White (Kluwer Academic/Plenum Publishers, New York, NY, 2002) p. 27.
18. S. R. CHOI and J. P. GYEKENYESI, *ASME J. Eng. Gas Turbines & Power* **123** (2001) 277.
19. ASTM C 1161, "Annual Book of ASTM Standards," Vol. 15.01 (ASTM, West Conshohocken, PA, 2002).
20. ASTM C 1259, "Annual Book of ASTM Standards," Vol. 15.01 (ASTM, West Conshohocken, PA 2002).
21. ASTM C 1327, "Annual Book of ASTM Standards," Vol. 15.01 (ASTM, West Conshohocken, PA, 2002).
22. ASTM C 1421, "Annual Book of ASTM Standards," Vol. 15.01 (ASTM, West Conshohocken, PA, 2001).
23. Y. AKIMUNE, T. AKIBA and T. OGASAWARA, *J. Mater. Sci.* **30** (1995) 1000.
24. Y. HARA, K. MATSUBARA, K.-I. MIZUNO, T. SHIMAMORI and H. YOSHIDA, ASME Paper No. 98-GT-498.
25. A. P. BORESI, O. M. SIDEBOTTOM, F. B. SEELY and J. O. SMITH, in "Advanced Mechanics of Materials" 3rd edn. (John Wiley & Sons, NY, 1978) p. 369; also see any text books of advanced mechanics of solids.
26. M. V. NATHAL and S. L. DRAPER, "National Aeronautics & Space Administration" (Glenn Research Center, Cleveland, OH, 2002).
27. S. R. CHOI, J. E. RITTER and K. JAKUS, unpublished work (University of Massachusetts, Amherst, MA, 1988).

Received 22 December 2003
and accepted 11 May 2004